The First Hillslope Thermokarst Inventory for the Permafrost Region of the Qilian Mountains

Xiaoqing Peng[1,3], Guangshang Yang[1], Oliver W. Frauenfeld[2], Xuanjia Li[1], Weiwei Tian[1], Guanqun Chen[1], Yuan Huang[1], Gang Wei[1], Jing Luo[4], Cuicui Mu[1,3],Fujun Niu[4]

[1]Key Laboratory of Western China's Environmental Systems (Ministry of Education), College of Earth and Environmental Sciences, Lanzhou University, Lanzhou, 730000, China
[2]Department of Geography, Texas A&M University, College Station, TX 77843-3147, USA
[3]Observation and Research Station on Eco-Environment of Frozen Ground in the Qilian Mountains, Lanzhou University, Lanzhou 730000, China
[4]State Key Laboratory of Frozen Soil Engineering, Northwest Institute of Eco-Environment and Resources, Chinese Academy of Sciences, Lanzhou 730000, China
* Corresponding author: Guangshang Yang (220220948511@lzu.edu.cn)

Abstract:

Climate warming and anthropogenic disturbances result in permafrost degradation in cold regions, including in the Qilian Mountains. These changes lead to extensive hillslope thermokarst (HT) formation, such as retrogressive thaw slumps, active-layer detachment slides, and thermal erosion gullies. These in turn cause, e.g., degradation of local vegetation, economic losses, infrastructure damages, and threats to human safety. However, despite its importance, there is currently no thermokarst inventory for the Qilian Mountains. Through manual visual interpretation and field validation, we therefore produce the first quantification of HT features. We count a total of 1064 HT features, with 67% located in the upper reaches of the Heihe River Basin, which encompasses ~13% of the Qilian Mountains region. We further identified that 187 HT features (18%) existed before 2010, while the remaining 874 (82%) were initiated in the recent period. More specifically, 392 sites (37%) were initiated during 2010–2015, and 482 (45%) after 2015. Thermokarst terrain is observed primarily in areas with shallow active layer depths (average thickness: 2.98 m) on northern shaded slopes of 3–25°, with low solar radiation and moderate elevations ranging from 3200 to 4000 m. This first inventory of HT features is an important and missing piece in documenting changes on the Qinghai-Tibetan Plateau, and this new dataset also provides an important basis for further studies, such as automated extraction of HT features, susceptibility analysis of HT, and estimating losses caused by HT. The datasets are available from the National Tibetan Plateau/Third Pole Environment Data Center and can be downloaded from https://doi.org/10.11888/Cryos.tpdc.300805 (Peng and Yang, 2023).

1 Introduction

The Qilian Mountains are located in the northeastern part of the Qinghai-Tibetan Plateau, at the confluence of three major geographical regions that include the eastern monsoon zone, the northwestern arid zone, and the alpine zone of the Qinghai-Tibetan Plateau. The Qilian Mountains play an important role in maintaining the ecological balance of the Tibetan Plateau, stopping the southward progression of deserts, and maintaining the stability of the oases in the Hexi Corridor. Due to its unique geographical and environmental characteristics, permafrost is widespread and underlies about 50% of the area (Ran et al., 2021). Permafrost has an important role in storing frozen water, thereby contributing to water conservation (Wang et al., 2022). These roles can aid in inland river runoff recharge, which is crucial to regional ecology, production, and life. Due to climate warming and human activities, significant permafrost degradation results in the frequent occurrence of thermokarst, representing a serious threat to ecological security and adversely impacts the environment and human beings (Li et al., 2022a).

Despite the importance of thermokarst processes and their potential geohazards, the distribution of thermokarst landscapes is currently mostly undocumented. The available distribution of thermokarst in the Northern Hemisphere, including retrogressive thaw slumps (RTSs), thermokarst lakes, and other terrain features, represents mainly probabilistic estimates (Olefeldt et al., 2016; Yin et al., 2021; Huang et al., 2023; Yang et al., 2023). Muster et al. (2017) determined the distribution of circumpolar Arctic permafrost lakes and ponds from 2002–2013 at a resolution of 5 m using optical remote sensing, satellite (Geo-Eye, QuickBird, WorldView-1 and -2, KOMPSAT-2), and radar imagery (TerraSAR-X), but temporal inconsistencies make comparisons in time and space difficult. At the regional scale, the techniques and spatial resolution of remote sensing imagery currently used at different study areas are inconsistent, e.g., estimating the distribution and development of RTSs on Banks Island, Canada, based on the interpretation of a Google Earth Engine Timelapse dataset (Lewkowicz and Way, 2019). Satellite imagery at 30-m resolution from Landsat has been used to analyze RTSs and thermokarst lakes in the region of Alaska within the circumpolar Arctic, eastern Canada, and Siberia (Nitze et al., 2018). Nicu et al. (2023) employed orthorectified imagery with a resolution of 5 meters to visually interpret and identify cryospheric hazards (such as thaw slumps and thermo-erosion gullies) in Nordenskiöld Land, covering an approximate area of 4000 square kilometers in the Svalbard Archipelago. The permafrost zone of the Qinghai-Tibetan Plateau (QTP) has been a site of thermokarst geomorphology research in recent years. For example, combining field surveys and SPOT-5 satellite data for August 2010, a total of 2,163 thermokarst lakes and ponds were recorded within 10 km on either side of the Chumar River to Fenghuo Mountain of the Qinghai-Tibet Railway, with a total surface area of 1.09×10^7 m^2 and ranging in size from 100 m^2 to 4.49×10^5 m^2 (Luo et al., 2015; Niu et al., 2014). In the Beiluhe region of the central QTP, the number of RTSs increased from 124 to 438 between 2008 and 2017, with an approximate 9-fold increase in area (Huang et al., 2020; Luo et al., 2019). The latest results show that the number of RTSs on the QTP is 2669, but for the Qilian Mountains in the northeastern part of the region, only 6 (Luo et al., 2022) or as many as 15 are documented (Mu et al., 2020). A lack of a thermokarst inventory in this region is therefore evident, representing a crucial gap in the RTSs inventory on the QTP.

Frequent occurrence of hillslope thermokarst hazards due to permafrost degradation,

with significant ecological impacts on the Qilian Mountains. The ecological environment of the permafrost areas has a significant impact, and there is a direct correlation between human activities and major permafrost engineering problems, including uneven subsidence of infrastructure, slumps, and cracks. Meanwhile, there is little to no information regarding hillslope thermokarst (HT) features such as RTSs, active-layer detachment slides, and thermo-erosion gullies (Gooseff et al., 2009) in the Qilian Mountains. HT refers to a specific type of thermokarst formation that occurs in permafrost regions. While it is similar to regular thermokarst, what distinguishes hillslope thermokarst is its occurrence on sloped terrain or hillsides, where permafrost thaw leads to slope instability. This can result in various landforms like retrogressive thaw sumps, thermo-erosion gullies, or active layer detachments, affecting the stability and shape of hillslopes in permafrost regions. These features can significantly impact the landscape and have implications for infrastructure, ecosystems, and land use in areas affected by hillslope thermokarst processes (Kokelj and Jorgenson, 2013; Olefeldt et al., 2016; Gooseff et al., 2009). Thus, the urgent need to survey and quantify these undocumented HT features in the Qilian Mountains motivates and represents the goal of this study.

2 Study Area

The Qilian Mountains are located at the northern edge of the QTP, with an average elevation of 3855 m. The region is underlain by permafrost and seasonally frozen ground (36–40°N and 94–104°E, Figure 1a), with a permafrost area of 94,235 km^2 that accounts for 49% of the study domain. Characterized by both an alpine mountain climate and a temperate continental monsoon climate, the mean annual air temperature is 0.30°C (Jin et al., 2022) with high precipitation variability and higher amounts in the southeast during the thawing season of June to September (Chen et al., 2013; Li et al., 2022b). Due to human activities, climate change, and earthquakes, permafrost instability in Qilian Mountains has gradually increased, resulting in HT formation including RTSs, active-layer detachment slides, and thermal erosion gullies, which pose a direct threat to the local economy, ecology, and safety.

121
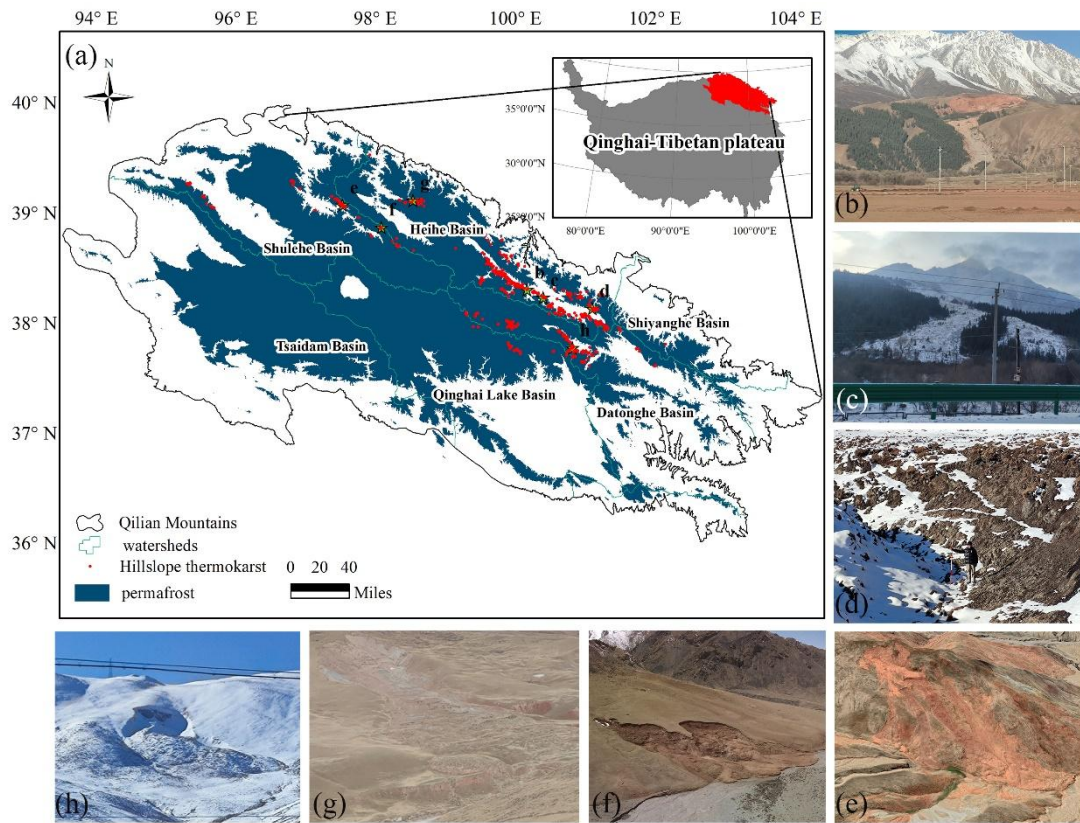
Figure 1 The location of the study area and a) its HT distribution (Qilian Mountains
permafrost extent data is from Sheng et al., 2020), and b)–h) HT features obtained
from different watersheds during our field surveys with the exception of e) a Google
Earth image, as this site is too difficult to access, the positions corresponding to b)–h)
have been labeled in a).

3 Data Sources

We collected and collated validated satellite imagery available starting in 1999 for
temporal detection of the onset of the HT formation. These data include unmanned
aerial vehicle imagery (e.g., Figure 1b–h) and 30 m resolution digital elevation model
data from the Shuttle Radar Topography Mission (Farr et al., 2007). A combination of
Omap and Google Earth software was used to detect the location of HT occurrence,
and Wayback imagery provided by ESRI was used to access high-resolution (<1 m)
satellite imagery and Jilin-1 satellite imagery (0.75 m) provided free of charge by
China Commercial Satellite Corporation to aid in the identification (Table 1). In
addition, we used digital elevation model data to calculate variables such as slope and
topographic position index (TPI) of the HT. The TPI is calculated as follows (YU
Hong, 2001):

$$\text{TPI} = \log_{10}\left(\frac{E}{Mean\,E} + 1\right) \times \left(\frac{S}{Mean\,S} + 1\right) \quad (1)$$

where E is the elevation (m), S is the slope (°), and *Mean* indicates that the mean
value for the entire Qilian Mountain region is used.

To further analyze the distribution of HT and the analogous environmental variables,
we obtain seismic data from the U.S. Geological Survey
(https://earthquake.usgs.gov/earthquakes/search/) describing earthquakes, including

their timing, epicenter location, and magnitude. To categorize vegetation types into deciduous-coniferous forests (DCF), undergrowth (U), alpine scrub meadow (ASM), alpine meadow (AM), alpine grassland (AG), alpine vegetation (AV), and non-vegetated area (NA), based on data from the Resource and Environment Science and Data Center (https://www.resdc.cn/data.aspx?DATAID=122). To assess the relationship of air temperature and precipitation with HT, we download monthly mean air temperature and precipitation at 2 m above ground level from the fifth generation of the European Centre for Medium-Range Weather Forecasts (ECMWF) reanalysis (ERA5; https://cds.climate.copernicus.eu/cdsapp#!/dataset/reanalysis-era5-land-monthly-means?tab=overview).
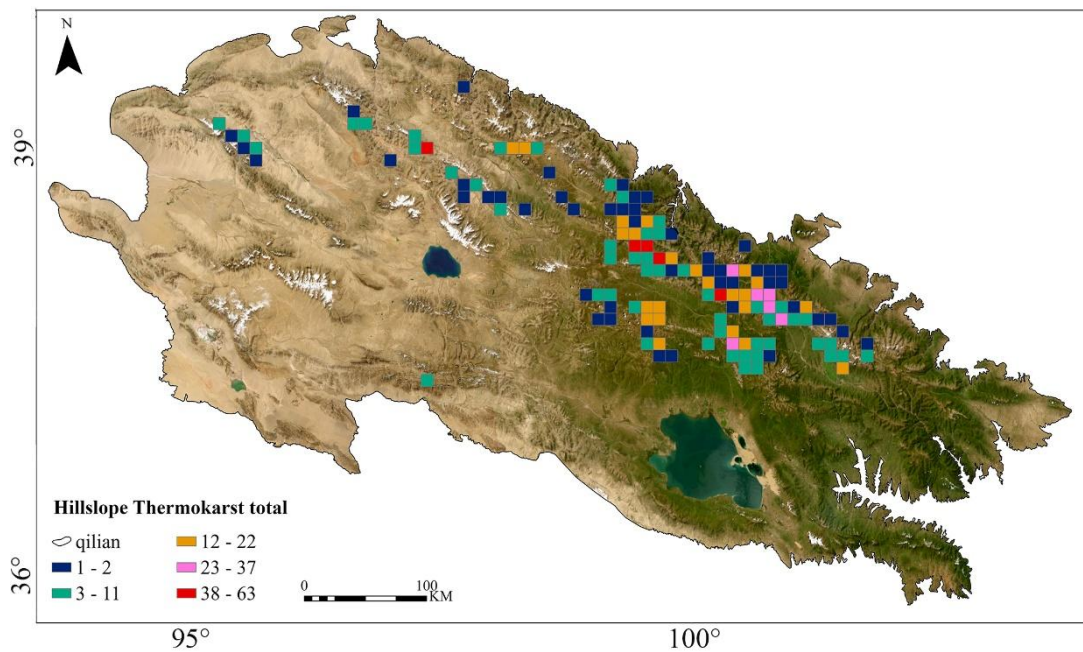
Figure 2 Frequency distribution of HT on the Qilian Mountains. The concentration of HT features is shown per 100 km^2 grid cell.

4 Methods

4.1 Manual Mapping

We first quantified and mapped HT via remote sensing observations. Most occurrences of HT in the permafrost region of the Qilian Mountains since 2000 were compiled by visual interpretation in Google Earth Pro and Omap. They were also aided by high resolution (<1 m) observations from Esri Wayback Imagery, which archives all published versions of world imagery (Table 1). We used a fishnet with a mesh size of 1×1 km to segment the latest satellite imagery for the entire Qilian Mountains to quantify HT mesh by mesh. RTSs are often horseshoe shaped, tongue shaped, elongated, branched, and circle chair-shaped (Lantuit and Pollard, 2008; Yin et al., 2021), characterized by a steep backwall, low-angle bottom, and a tongue of displaced saturated soil (Lantz and Kokelj, 2008; Nicu et al., 2021). These features are tonally and morphologically different from their surroundings in color satellite images during the thawing season. RTSs also produce folded textures due to soil

accumulation, which appear as laterally folded stripes on imagery. Active-layer detachment slides are a common shallow landslide in permafrost areas. Their morphological characteristics vary based on vegetation cover, slope, and permafrost conditions, but common features include highly disturbed slopes, lateral shear zones, and fracture zones formed after the sliding of the active layer (Lewkowicz, 2007). We detected and sketched these features based on morphological, tonal, textural, shading, and other characteristics on remote sensing images, and then digitized their morphological features into polygonal data. Although the accuracy of this type of visual interpretation is relatively high, some HT features can be missed via this manual interpretation. To reduce such errors, satellite images of the similar period from different sources were evaluated four times using the same methods to ensure accurate results. The date of the satellite image when perturbations caused by HT can be first observed was defined as the initiation year of a particular HT feature. Depending on the initiation year, HT is categorized as occurring before 2010, 2010–2015, or after 2015. To observe the temporal evolution of HT features, we used the initiation year and retraced historical images covering the Qilian Mountains, a process that also helped us distinguish between HT features and one-time transient landslides.

4.2 Field Verification

Similar HT can have different morphological characteristics due to different triggers. It is thus difficult to identify the type of HT simply through imagery. In addition, after an initial trigger and HT formation, thermokarst can evolve into different types. For example, active layer detachment slides may transition into RTS due to the exposure of subsurface ice at the trailing edge and water erosion due to thawing, which can cause the RTS to further progress into mudflows. Therefore, with visual interpretation based on imagery only providing individual snapshots, it is essential to also conduct field surveys as a validation exercise. We conducted a total of three field surveys in winter 2022, and spring and summer of 2023. Field work covered the Shiyanghe basin, Heihe basin, Datonghe basin, Qinghai Lake basin, and Shulehe basin. Due to the harsh climatic conditions and accessibility issues in the Qilian Mountains, unmanned aerial vehicles were used to survey and verify hard-to-reach areas.

Table 1 List of the data used for manual interpretation and mapping of HT features.

Software Platform	Time Span	Resolution	Data Sources
Google Earth pro	1999–2022	0.6–15 m	Quickbird, IKONOS, etc.
Omap	since 2021	<1 m	GF-2
ESRI World Imagery	since 2014	<1 m	WordView-3, WordView-4, etc.
Jilin-1 website	2022	0.75 m	Jilin-1
UAV images	Feb., Apr., May 2023	~15 cm	Field Surveys

4.3 Morphological and Spatial Statistical Analysis

A landscape shape index (LSI) can be quantified to characterize shape complexity by calculating the degree of deviation of a given patch from a circle or square of the

same area. To quantify the shape characteristics of HT features, two LSIs are calculated as follows:

$$LSI_{square} = \frac{0.25P}{\sqrt{A}} \quad (2)$$

$$LSI_{round} = \frac{P}{2\sqrt{\pi A}} \quad (3)$$

where P is the perimeter (m) and A is the area (m^2). The closer the values of LSI$_{square}$ or LSI$_{round}$ are to 1, the more square or round the shape of the HT feature is, respectively.

To further investigate the spatial distribution of HT, we computed a global Moran's index, z-score, and p-value to determine whether there is autocorrelation in the spatial distribution of HT, where p-values of z-scores are used to measure statistical significance. When p-value < 0.01 and z-score > 2.58, there is a 99% probability that HTs are clustered within the study area. The smaller the p-value and the larger the z-score, the greater the probability that such spatial patterns are clustered. Moran's index ranges from −1 to 1, with negative values corresponding to negative correlations, positive values to positive correlations, and 0 denotes that the spatial objects in the study area are independent of each other. Additionally, the closer the index is to 1, the more clustered the HT features are, and the closer of the index is to −1, the more dispersed the HT features are. To delineate the regions that may have spatial autocorrelation (Bivand and Wong, 2018), we further process local autocorrelation on this basis. The local autocorrelation regions are divided into four types based on the local Moran's index: High-High (HH) clustering, High-Low (HL) clustering, Low-High (LH) clustering, and Low-Low (LL) clustering. HH signifies a region with both a higher amount of HT and neighboring regions also having a higher amount of HT; HL indicates a region with a higher amount of HT surrounded by neighboring regions with a lower amount of HT; LH indicates a region with a lower amount of HT neighboring areas with a higher amount of HT; and LL represents a region with both a lower amount of HT and neighboring regions with a lower amount of HT. Although the methods described above can identify global and local spatial autocorrelation, respectively, they are unable to identify clusters of concentrated HT features. We therefore also apply hot spot analysis, which is another effective way of exploring the characteristics of local spatial distributions. All the above techniques are based on spatial statistical analysis functions in ArcGIS.

To explore the effects of climate on HT, we obtained the monthly mean air temperature and precipitation at 2 meters above ground level from ERA5 over the period 2000–2020 and calculate their annual spatial means and standard deviations (Figure 6).
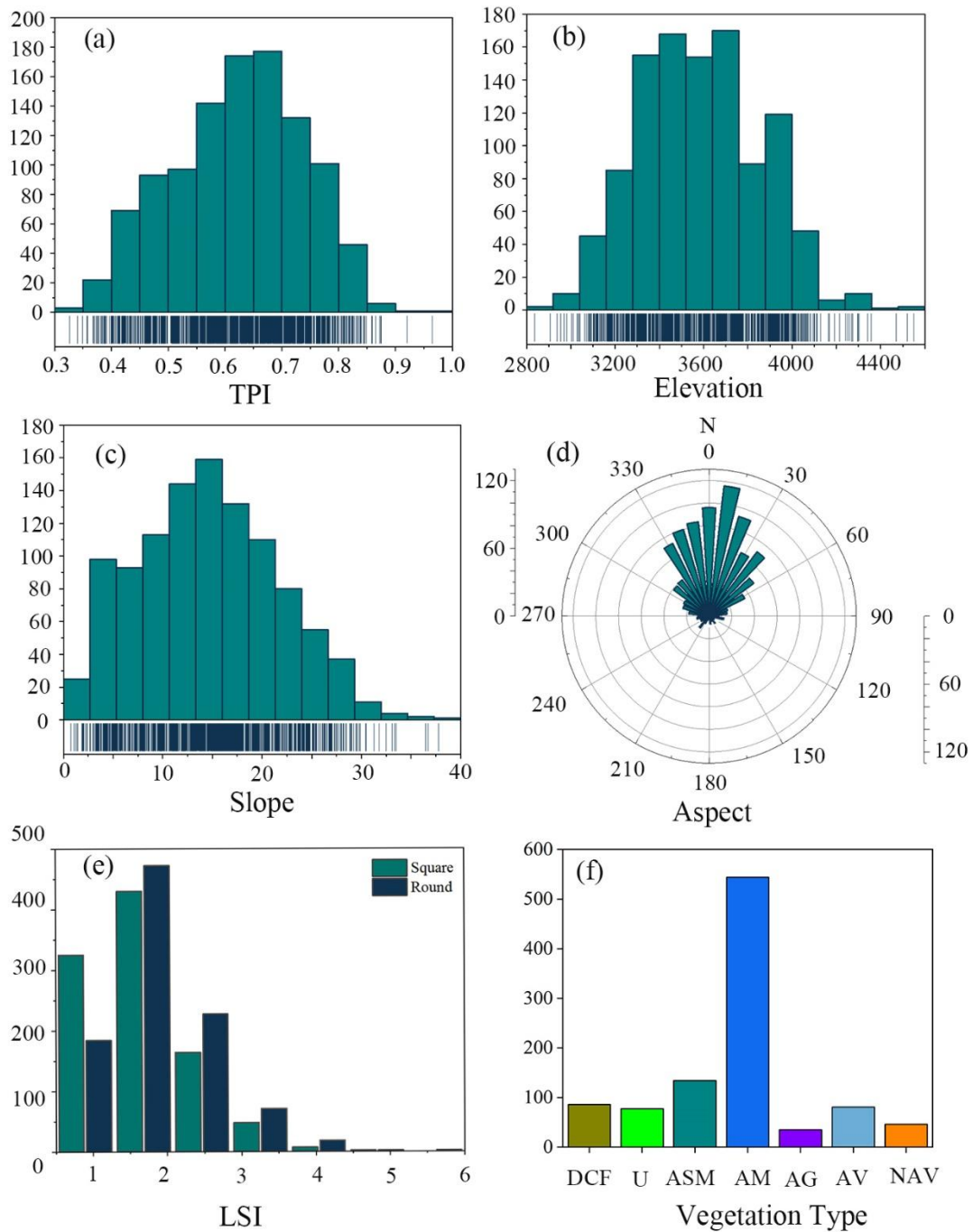
Figure 3 The number of HT terrain features (y-axes) of HT as categorized by (a) topographic position index (TPI), (b) elevation, (c) slope, (d) aspect, (e) landscape shape index (LSI), and (f) vegetation type including deciduous coniferous forests (DCF), undergrowth (U), alpine scrub meadow (ASM), alpine meadow (AM), alpine grassland (AG), alpine vegetation (AV), and non-vegetated area (NA); the blue vertical lines at the bottom of panels a–c represent the number of HT features in each x-axis bin.

5 Results

261   Our inventory of HT includes the Heihe Basin, Shulehe Basin, Datonghe Basin,
262   Shiyanghe Basin, Qinghai Lake Basin, and Tsaidam Basin within the Qilian
263   Mountains, with a total of 1064 HT features. In any 100 km^2 grid cell, the maximum
264   density of HT is 63 (Figure 2).This density is lower than the 68 per 25 km^2 in the
265   central Tibetan Plateau reported by (Luo et al., 2022) and 88 per 25 square km^2 on
266   Banks Island, Canada from (Lewkowicz and Way, 2019). 67% of these HT features
267   were identified in the Heihe River basin, followed by the Datonghe River Basin,
268   accounting for 19%. The HT distribution in these river basins is irregular,
269   corroborated by a positive statistically significant Moran's index value of 0.3, p-value
270   of 0.00001, and z-score of 32.5. Of all the HT features, the largest is 58 ha, the
271   smallest area is 0.01 ha, with most being smaller than 10 ha. The average area is 1.75
272   ha, with a total area of 1708 ha.

273   The spatial distribution of RTS on the QTP is strongly controlled by terrain factors
274   such as the elevation, slope, TPI, and aspect (Luo et al., 2022). The statistical results
275   indicate that HT is observed at elevations ranging from 2,835 to 4,550 m. However,
276   90% of HTs are more likely to occur at elevations ranging from 3,200 to 4,000 m in
277   the middle/high elevation area of the Qilian Mountains. HT tends to occur on
278   north-facing slopes (Figure 3b and 3d), with slopes ranging from 3° to 25° (Figure 3c).
279   In addition, the TPI shows that ~85% of the HTs occur mainly between 0.5 and 0.8
280   (Figure 3a), suggesting that they commonly occur in locations that are lower than
281   their surroundings. Both LSI indices suggest that 75% of HT has values close to 1.0
282   (Figure 3e), indicating that most HT is simple in shape and compact in morphology
283   (Niu et al., 2016). Alpine meadow areas contain ~53% of HT, followed by alpine
284   scrub meadows, which contain 13% (Figure 3f).

285   The initiation years of HT features are variable across the study area. 187 HT features
286   (18%) were identified before 2010, and the remaining 82% in the last 10 years. 392
287   sites (37%) were initiated in 2010–2015 and 482 (45%) after 2015. Much of the newly
288   initiated HT occurred in the Heihe basin and the middle and upper reaches of the
289   Datonghe basin (Figure 4), which is also a HT hotspot region. The recent increase in
290   HT can be attributed to the anomalous weather conditions in the corresponding years.
291   The association between newly observed HT and meteorological data indicates a
292   sudden HT increase in years with unusually high temperatures during the thawing
293   season (Figure 6).
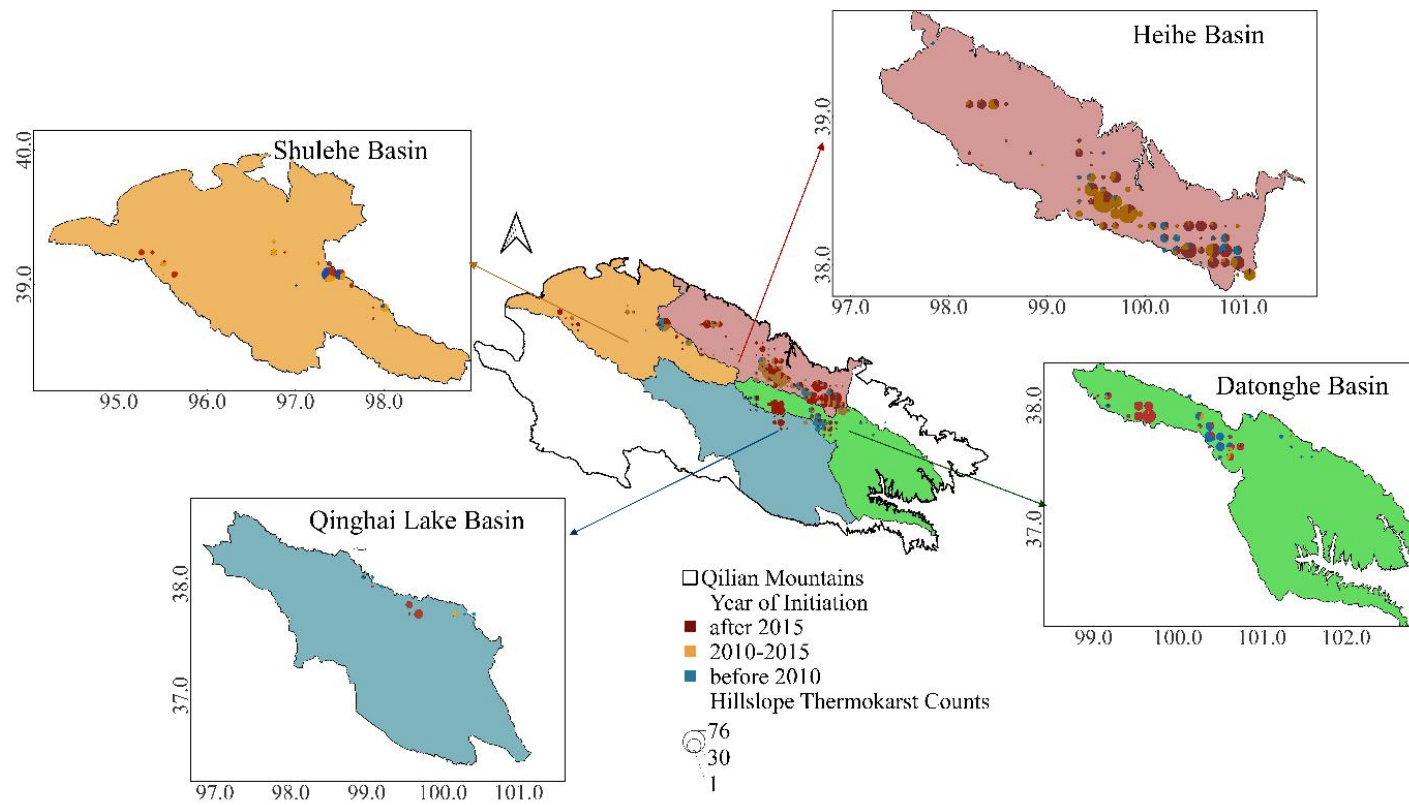
294
295 **Figure 4** The timing of HT initiation within 100 km² grid cells.
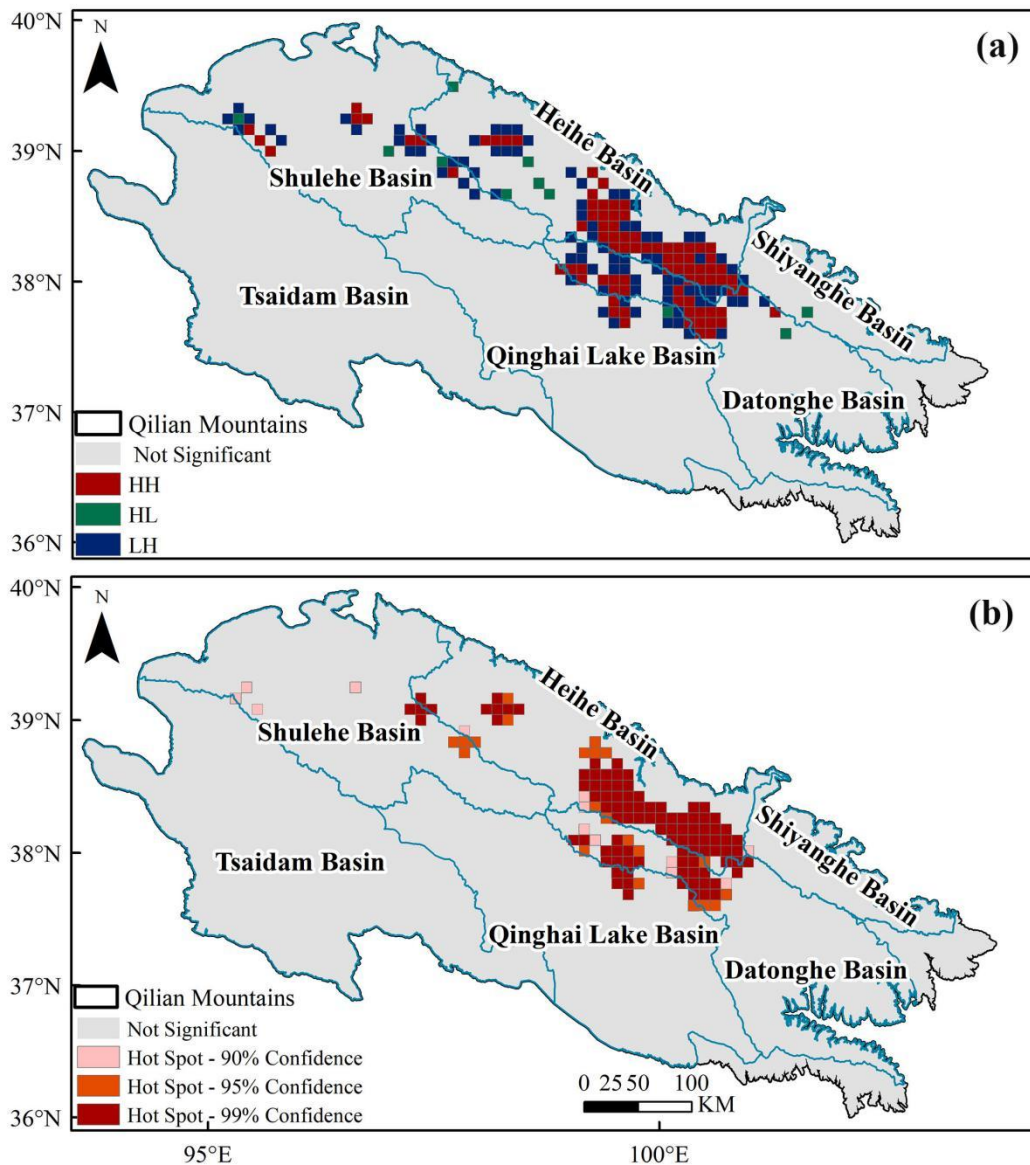
294
296
297 **Figure 5** (a) Spatial autocorrelation indicating high-high (HH), high-low (HL), and
298 low-high (LH) clustering, and (b) hotspot analysis where the different colors represent
299 the confidence levels.
300

6 Discussion

6.1 Drivers of HT in the Qilian Mountainous

6.1.1 Permafrost Conditions

Formation of HT is facilitated by thick subsurface ice and various internal and
external environmental conditions (Stephani et al., 2023). Permafrost stability in
~80% of the permafrost area of the Qilian Mountains is predominantly transitional,
and higher permafrost temperatures (Ran et al., 2021) will exacerbate the climate
sensitivity of this area (Lewkowicz and Way, 2019; Patton et al., 2021) leading to
melting of the subsurface ice and an increase in active layer thickness, thus decreasing
the stability of the slope (Behnia and Blais-Stevens, 2018). This is also supported by
our finding that ~90% of HT occurs in the transition zone between permafrost and

312 seasonally frozen soil where mean annual ground temperature is greater than −1°C.
313
314 *6.1.2 Environmental Factors*

315 Topographic conditions facilitate the formation of subsurface ice and the continuous
316 development of HT. At elevations below 5100 m on the QTP, aspect dominates the
317 distribution of permafrost. More permafrost underlies regions of shaded, north-facing
318 slopes than sunny south-facing slopes (Ran et al., 2021). Indeed, we find that ~95% of
319 Qilian Mountain HT is found on north-facing slopes where it also enhances vegetation
320 growth and soil moisture storage (Jin et al., 2009). Lower solar radiation, higher
321 permafrost ice content, and shallow active layer thickness (Lacelle et al., 2015; Ward
322 Jones et al., 2019) also enables HT formation (Luo et al., 2022; Niu et al., 2016; Xia
323 et al., 2022). We find more than half of the HT occurs in alpine meadows, which
324 require more water content than alpine steppes (Yin et al., 2017) and consequently
325 also results in more ground ice development under this vegetation type. We
326 determined that ~90% of HT in the Qilian Mountains occurs on 3° to 25° slopes. Low
327 and gentle slopes are favorable for groundwater pooling (Luo et al., 2022), whereas
328 slopes greater than 16° are relatively steep and therefore not conducive to
329 groundwater enrichment for ice formation, but such slopes also provide dynamic
330 conditions for active layer detachments and collapsing ground (Wang, 1990). We also
331 observe more HT initiation at locations that are lower compared to their surroundings,
332 as such depressions favor the accumulation of snow and rainwater (Stieglitz et al.,
333 2003) and prevent heat loss from the soil. This encourages melting of subsurface ice
334 (Zhang, 2005) at the base of the active layer and, after an unstable layer is formed
335 between the permafrost and the active layer, the overlying soil can slide along the
336 slope (Patton et al., 2021).

337 The Qilian Mountains were and are still formed by the ongoing collision of the Indian
338 Ocean Plate and the Eurasian Plate, resulting in the Qilian Mountains-Hexi Corridor
339 active fault system (Xiong et al., 2017) that has seen nearly 400 earthquakes of
340 magnitude 2 or greater over the past two decades. In particular, the high seismic
341 activity of the Heihe, Shiyanghe, and Datonghe Basins (Figure 7a) represents a
342 potential threat to the safety and integrity of current and future infrastructure in the
343 region. During our field investigations we found a nearly 3 km long and 2 m deep
344 slope fracture caused by a 6.9-magnitude earthquake in 2022, resulting in a massive
345 exposure of subsurface ice and the collapse of the Lanzhou-Xinjiang High Speed Rail
346 Tunnel (Figure 7b and c). The occurrence of an earthquake can result in an
347 instantaneous increase in pore water pressure and sliding forces that reduce slope
348 stability and potentially leads to a massive exposure of subsurface ice (Niu et al., 2016;
349 Xia et al., 2022), sediment liquefaction (Dadfar et al., 2017), and permafrost warming
350 due to the seismic vibrations. These vibrations lead to cracking and deformation of the
351 ice layers within the permafrost, releasing moisture and heat, consequently resulting
352 in a temperature rise of the permafrost. Additionally, earthquakes can induce the flow
353 of pore water within the permafrost, further influencing its temperature (Che et al.,
354 2014), creating the ideal setting for active-layer detachment slides. The clustering of
355 earthquake activity in the lower left corner of Figure 7a is not associated with HT
356 features, because there is no permafrost in this region.
357
358 *6.1.3 Climate Factors*

359 Extreme summer temperatures and precipitation have been identified as triggers for
360 the initiation of RTSs in many Arctic permafrost zones (Balser et al., 2014; Kokelj et

al., 2015; Lewkowicz and Way, 2019; Segal et al., 2016). Given our finding that 82% of HT was initiated in approximately the last decade (Figure 4), mostly during 2010-2015 and after 2015, we used ERA5 to determine the temperature and precipitation characteristics for the Qilian Mountains over the last 20 years (Li et al., 2022b) (Figure 6, the square symbols). The mean thawing season air temperatures in 2010 and 2016 were higher than in other years (Figure 6a, red square symbols). A warming thaw season could lead to thaw consolidation at the base of the active layer or to higher porewater pressure in the transient thaw layer, reducing the effective shear strength, and causing slope failure (Lewkowicz and Way, 2019). The anomalous air temperatures during the thawing season could accelerate permafrost thaw and expose ice-rich permafrost, thus leading to new HT (Figure 6a, dark brown and dark red bars, respectively). Rainfall infiltration may transfer heat to the top layer of permafrost and induce melting of ground ice in ice-rich transient layers, which would increase the porewater pressure at the active layer-permafrost interface and thereby trigger formation of HT (Luo et al., 2022). However, precipitation variability during the thawing season does not match HT formation (Figure 6b). Despite high precipitation in both 2007 and 2018 (Figure 6b, blue squares), no initiation of HT was found to subsequently coincide with these peaks (blue squares), and precipitation also does not explain the significant initiation of HTs between 2010-2015, nor after 2015 (Figure 6b, yellow and red bars, respectively). The same conclusion also applies to the other three sub-regions—Hoh Xil Mountain, Maqu county, and Honglianghe—and it could be speculated that the nature of the soils on the QTP may instead play a role (Luo et al., 2022).
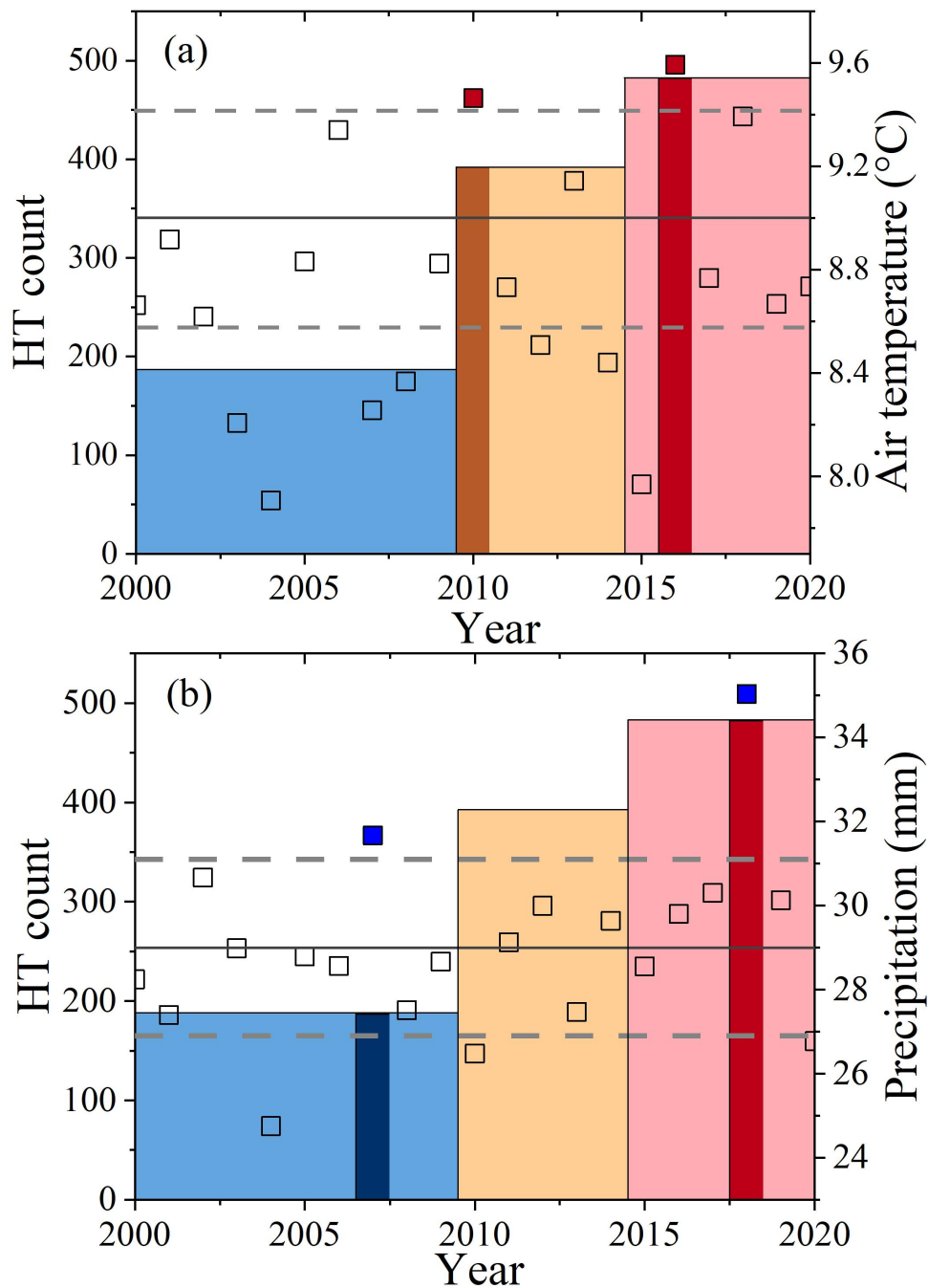
Figure 6 The relationship between HT numbers (variable-width bars, the darker colors represent years with extreme weather events) and (a) temperature and (b) precipitation in the thawing season from 2000 to 2020 (square symbols, the red squares and the blue squares represent the extreme weather events). The solid horizontal line represents the mean air temperature and precipitation, respectively, and the dashed lines represent ±1 standard deviation.

6.1.4 Human Activities

Extensive and increasing human activities have been shown to significantly accelerate permafrost degradation (Cheng & Jin, 2013; IPCC, 2019). The total population of the Qilian Mountains is about 60,000, there are approximately 1,000 metal, energy, and other types of mineral deposits (National Mineral Properties Database 2021 Edition,

http://data.ngac.org.cn/mineralresource/index.html), and there are ~8,000 km of railroads and highways. The core of this human activity is concentrated on the eastern side of the Qilian Mountains, which generally coincides with the spatial distribution of the HT hotspots we documented. This qualitatively suggests a role of human activities on HT from, e.g., engineering disturbances, vegetation degradation due to overgrazing, etc. (Sharkhuu et al., 2007). Establishing the impact of human activities on HT quantitatively is still a difficult challenge, but our identification of the location and timing of HT formation is a first, important step for further future studies, especially on the socioeconomic development in the region.
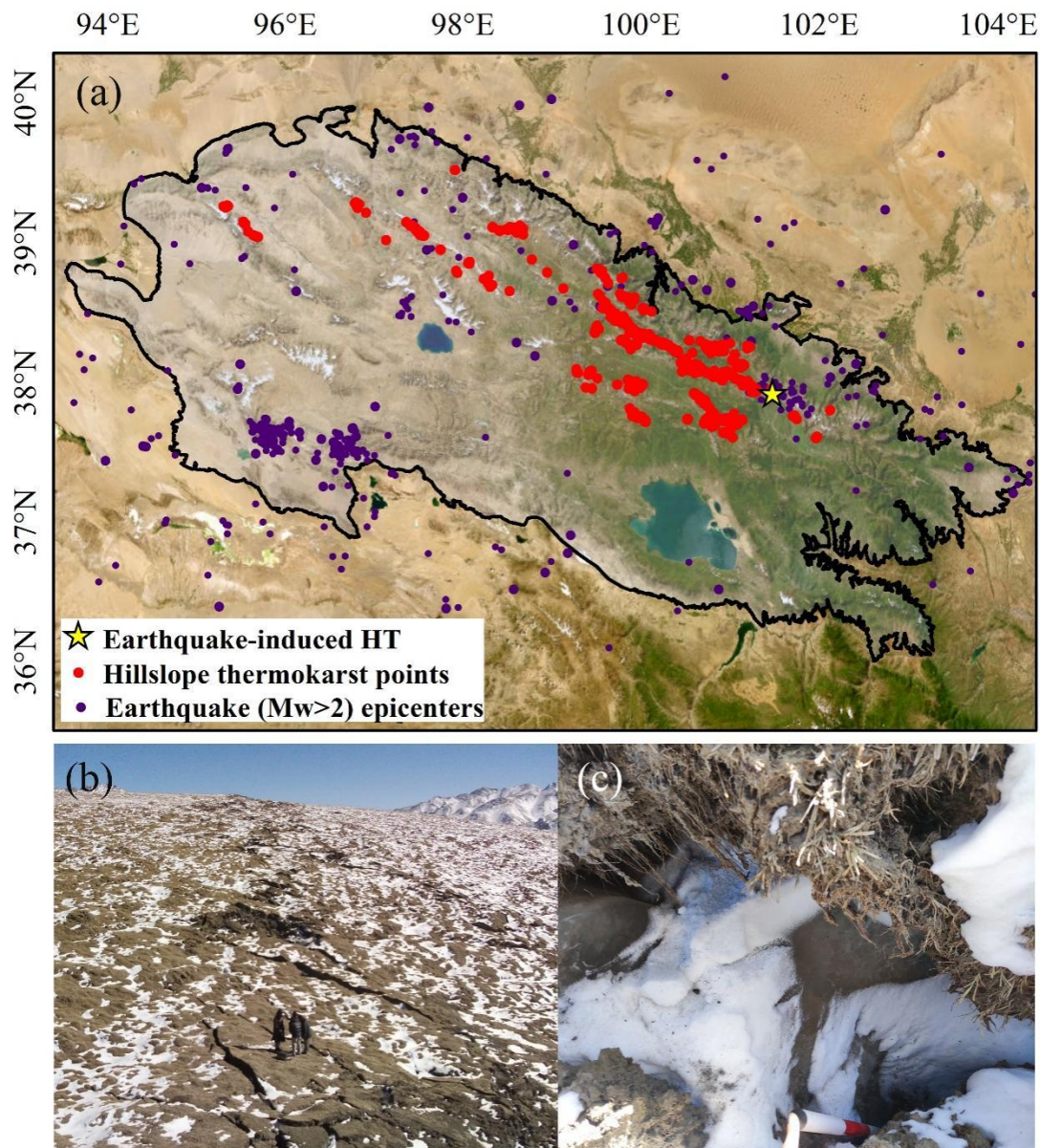
Figure 7 Qilian Mountains showing (a) the location of HT locations and earthquakes with magnitude >2 in the last 20 years, (b) slope fractures caused by earthquakes, and (c) exposed subsurface ice.

7 Data Availability

DEM data can be accessed through NASA

(https://www.earthdata.nasa.gov/sensors/srtm). Landsat5-8 data are available from USGS (https://www.usgs.gov/) and Sentinel-2 from ESA (https://www.esa.int/), and can be downloaded through Google Earth Engine. Esri World Imagery can be accessed through Esri Wayback Imagery at: https://livingatlas.arcgis.com/wayback. Some GF-2 imagery is also available online through Omap software (https://www.ovital.com/283-2/), and high-resolution 3D satellite imagery of the Qilian Mountain region can be viewed in Google Earth software. High-resolution satellite images captured by the Jilin-1 satellite in China can be viewed by accessing https://www.jl1mall.com/rskit/. The HT inventory for the Qilian Mountains can be freely downloaded from the National Tibetan Plateau/Third Pole Environment Data Center (https://doi.org/10.11888/Cryos.tpdc.300805, Peng and Yang, 2023).

8 Conclusion

This study used visual interpretation and field investigations with repeated verification to investigate HT in the permafrost zone of the Qilian Mountains. We successfully produced the first HT inventory for this area, identifying a total of 1064 HT features. The area of these features ranged from 0.01 to 58 ha, with an average of 1.75 ha. Thermokarst is primarily concentrated at the junction between the upstream portion of the Heihe River Basin and the mid and upstream portion of the Datonghe Basin. Within a 10×10 km area, thermokarst has a maximum density of 63 features, affecting an area of ~20 km^2. HT in the Qilian Mountains is more likely to occur on north-facing shaded slopes, at elevations between 3200–4000 m, slopes of 3–25°, 0.5<TPI<0.8, and in alpine meadow vegetation. Based on long-term satellite imagery, 874 new HT features were initiated after 2010, accounting for 82% of all HT features. Of these, 392 and 482 were initiated during the periods of 2010–2015 and after 2015, respectively. Recent higher air temperatures during the thawing season are likely important reasons for the intensification of HT formation in the Qilian Mountains, while precipitation does not seem to play a role. This first HT inventory for the Qilian Mountains will be fundamental for quantitative assessments that explore the exact causes and underlying thermokarst processes, providing observational data support for automated extraction of HT features, and ultimately enhance the identification and prediction of regions prone to thermokarst processes in the future. Furthermore, it will facilitate the evaluation of local risk levels, potential economic losses, population casualties, and other impacts, thereby furnishing governmental decision-makers and relevant stakeholders with essential reference materials for mitigating potential risks.

Author contributions. XP and GY designed the research and obtained funding. GY analyzed the data and prepared the data files. GY, WT, XL and XP conducted the field work. GY, XP, OWF, JL, CM, FN wrote the paper with input from the coauthors and coordinated the analysis and contributions from all coauthors. XP and GY contributed to the work equally and should be regarded as co-first authors.

Competing interests. The contact author has declared that neither they nor their coauthors have any competing interests.

Disclaimer. Publisher's note: Copernicus Publications remains neutral with regard to jurisdictional claims in published maps and institutional affiliations.

Acknowledgements

This work was supported by the Second Tibetan Plateau Scientific Expedition and Research Program (STEP) (2019QZKK0905), the National Natural Science Foundation of China (42161160328, 42171120), and the Fundamental Research Funds for the Central Universities (lzujbky-2023-01).

References

Balser, A. W., Jones, J. B., and Gens, R.: Timing of retrogressive thaw slump initiation in the Noatak Basin, northwest Alaska, USA, J. Geophys. Res. Earth Surf., 119, 1106–1120, https://doi.org/10.1002/2013JF002889, 2014.

Behnia, P. and Blais-Stevens, A.: Landslide susceptibility modelling using the quantitative random forest method along the northern portion of the Yukon Alaska Highway Corridor, Canada, Nat. Hazards, 90, 1407–1426, https://doi.org/10.1007/s11069-017-3104-z, 2018.

Bivand, R. S. and Wong, D. W. S.: Comparing implementations of global and local indicators of spatial association, TEST, 27, 716–748, https://doi.org/10.1007/s11749-018-0599-x, 2018.

Che, A., Wu, Z., and Wang, P.: Stability of pile foundations base on warming effects on the permafrost under earthquake motions, Soils Found., 54, 639–647, https://doi.org/10.1016/j.sandf.2014.06.006, 2014.

Chen, H., Zhu, Q., Peng, C., Wu, N., Wang, Y., Fang, X., Gao, Y., Zhu, D., Yang, G., Tian, J., Kang, X., Piao, S., Ouyang, H., Xiang, W., Luo, Z., Jiang, H., Song, X., Zhang, Y., Yu, G., Zhao, X., Gong, P., Yao, T., and Wu, J.: The impacts of climate change and human activities on biogeochemical cycles on the Qinghai-Tibetan Plateau, Glob. Change Biol., 19, 2940–2955, https://doi.org/10.1111/gcb.12277, 2013.

Cheng, G. and Jin, H.: Permafrost and groundwater on the Qinghai-Tibet Plateau and in northeast China, Hydrogeol. J., 21, 5–23, https://doi.org/10.1007/s10040-012-0927-2, 2013.

Dadfar, B., El Naggar, M. H., and Nastev, M.: Quantifying exposure of linear infrastructures to earthquake-triggered transverse landslides in permafrost thawing slopes, Can. Geotech. J., 54, 1002–1012, https://doi.org/10.1139/cgj-2017-0076, 2017.

Farr, T. G., Rosen, P. A., Caro, E., Crippen, R., Duren, R., Hensley, S., Kobrick, M., Paller, M., Rodriguez, E., Roth, L., Seal, D., Shaffer, S., Shimada, J., Umland, J., Werner, M., Oskin, M., Burbank, D., and Alsdorf, D.: The Shuttle Radar Topography Mission, Rev. Geophys., 45, https://doi.org/10.1029/2005RG000183, 2007.

Gooseff, M. N., Balser, A., Bowden, W. B., and Jones, J. B.: Effects of Hillslope Thermokarst in Northern Alaska, Eos Trans. Am. Geophys. Union, 90, 29–30, https://doi.org/10.1029/2009EO040001, 2009.

Huang, L., Luo, J., Lin, Z., Niu, F., and Liu, L.: Using deep learning to map retrogressive thaw slumps in the Beiluhe region (Tibetan Plateau) from CubeSat images, Remote Sens. Environ., 237, 111534, https://doi.org/10.1016/j.rse.2019.111534, 2020.

Huang, L., Willis, M. J., Li, G., Lantz, T. C., Schaefer, K., Wig, E., Cao, G., and Tiampo, K. F.: Identifying active retrogressive thaw slumps from ArcticDEM, ISPRS Journal of Photogrammetry and Remote Sensing, 205, 301–316, https://doi.org/10.1016/j.isprsjprs.2023.10.008, 2023.

Jin, H., Li, X., Frauenfeld, O. W., Zhao, Y., Chen, C., Du, R., Du, J., and Peng, X.: Comparisons of statistical downscaling methods for air temperature over the Qilian Mountains, Theor. Appl. Climatol., 149, 893–896, https://doi.org/10.1007/s00704-022-04081-w, 2022.

Jin, X., Wan, L., Zhang, Y.-K., Hu, G., Schaepman, M. E., Clevers, J. G. P. W., and Su, Z. B.: Quantification of spatial distribution of vegetation in the Qilian Mountain area with MODIS NDVI, Int. J. Remote Sens., 30, 5751–5766, https://doi.org/10.1080/01431160902736635, 2009.

Kokelj, S. V., Tunnicliffe, J., Lacelle, D., Lantz, T. C., Chin, K. S., and Fraser, R.: Increased precipitation drives mega slump development and destabilization of ice-rich permafrost terrain, northwestern Canada, Glob. Planet. Change, 129, 56–68, https://doi.org/10.1016/j.gloplacha.2015.02.008, 2015.

Kokelj, S. V. and Jorgenson, M. T.: Advances in Thermokarst Research: Recent Advances in Research Investigating Thermokarst Processes, Permafrost and Periglac. Process., 24, 108–119, https://doi.org/10.1002/ppp.1779, 2013.

Lacelle, D., Brooker, A., Fraser, R. H., and Kokelj, S. V.: Distribution and growth of thaw slumps in the Richardson Mountains–Peel Plateau region, northwestern Canada, Geomorphology, 235, 40–51, https://doi.org/10.1016/j.geomorph.2015.01.024, 2015.

Lantuit, H. and Pollard, W. H.: Fifty years of coastal erosion and retrogressive thaw slump activity on Herschel Island, southern Beaufort Sea, Yukon Territory, Canada, Geomorphology, 95, 84–102, https://doi.org/10.1016/j.geomorph.2006.07.040, 2008.

Lantz, T. C. and Kokelj, S. V.: Increasing rates of retrogressive thaw slump activity in the Mackenzie Delta region, N.W.T., Canada, Geophys. Res. Lett., 35, L06502, https://doi.org/10.1029/2007GL032433, 2008.

Lewkowicz, A. G.: Dynamics of active-layer detachment failures, Fosheim Peninsula, Ellesmere Island, Nunavut, Canada, Permafr. Periglac. Process., 18, 89–103, https://doi.org/10.1002/ppp.578, 2007.

Lewkowicz, A. G. and Way, R. G.: Extremes of summer climate trigger thousands of thermokarst landslides in a High Arctic environment, Nat. Commun., 10, 1329, https://doi.org/10.1038/s41467-019-09314-7, 2019.

Li, Y., Qin, X., Liu, Y., Jin, Z., Liu, J., Wang, L., and Chen, J.: Evaluation of Long-Term and High-Resolution Gridded Precipitation and Temperature Products in the Qilian Mountains, Qinghai–Tibet Plateau, Front. Environ. Sci., 10, 906821, https://doi.org/10.3389/fenvs.2022.906821, 2022.

Luo, J., Niu, F., Lin, Z., Liu, M., and Yin, G.: Thermokarst lake changes between 1969 and 2010 in the Beilu River Basin, Qinghai–Tibet Plateau, China, Sci. Bull., 60, 556–564, https://doi.org/10.1007/s11434-015-0730-2, 2015.

Luo, J., Niu, F., Lin, Z., Liu, M., and Yin, G.: Recent acceleration of thaw slumping in permafrost terrain of Qinghai-Tibet Plateau: An example from the Beiluhe Region, Geomorphology, 341, 79–85, https://doi.org/10.1016/j.geomorph.2019.05.020, 2019.

Luo, J., Niu, F., Lin, Z., Liu, M., Yin, G., and Gao, Z.: Inventory and Frequency of Retrogressive Thaw Slumps in Permafrost Region of the Qinghai–Tibet Plateau, Geophys. Res. Lett., 49, https://doi.org/10.1029/2022GL099829, 2022.

Mu, C., Shang, J., Zhang, T., Fan, C., Wang, S., Peng, X., Zhong, W., Zhang, F., Mu, M., and Jia, L.: Acceleration of thaw slump during 1997–2017 in the Qilian Mountains of the northern Qinghai-Tibetan plateau, Landslides, 17, 1051–1062, https://doi.org/10.1007/s10346-020-01344-3, 2020.

Muster, S., Roth, K., Langer, M., Lange, S., Cresto Aleina, F., Bartsch, A., Morgenstern, A., Grosse, G., Jones, B., Sannel, A. B. K., Sjöberg, Y., Günther, F., Andresen, C., Veremeeva, A., Lindgren, P. R., Bouchard, F., Lara, M. J., Fortier, D., Charbonneau, S., Virtanen, T. A., Hugelius, G., Palmtag, J., Siewert, M. B., Riley, W. J., Koven, C. D., and Boike, J.: PeRL: a circum-Arctic Permafrost Region Pond and Lake database, Earth Syst. Sci. Data, 9, 317–348, https://doi.org/10.5194/essd-9-317-2017, 2017.

Nitze, I., Grosse, G., Jones, B. M., Romanovsky, V. E., and Boike, J.: Remote sensing quantifies widespread abundance of permafrost region disturbances across the Arctic and Subarctic, Nat. Commun., 9, 5423, https://doi.org/10.1038/s41467-018-07663-3, 2018.

Niu, F., Luo, J., Lin, Z., Liu, M., and Yin, G.: Morphological Characteristics of Thermokarst Lakes along the Qinghai-Tibet Engineering Corridor, Arct. Antarct. Alp. Res., 46, 963–974, https://doi.org/10.1657/1938-4246-46.4.963, 2014.

Niu, F., Luo, J., Lin, Z., Fang, J., and Liu, M.: Thaw-induced slope failures and stability analyses in permafrost regions of the Qinghai-Tibet Plateau, China, Landslides, 13, 55–65, https://doi.org/10.1007/s10346-014-0545-2, 2016.

Nicu, I. C., Lombardo, L., and Rubensdotter, L.: Preliminary assessment of thaw slump hazard to Arctic cultural heritage in Nordenskiöld Land, Svalbard, Landslides, 18, 2935–2947, https://doi.org/10.1007/s10346-021-01684-8, 2021.

Nicu, I. C., Elia, L., Rubensdotter, L., Tanyaş, H., and Lombardo, L.: Multi-hazard susceptibility mapping of cryospheric hazards in a high-Arctic environment: Svalbard Archipelago, Earth Syst. Sci. Data, 15, 447–464, https://doi.org/10.5194/essd-15-447-2023, 2023.

Olefeldt, D., Goswami, S., Grosse, G., Hayes, D., Hugelius, G., Kuhry, P., McGuire, A. D., Romanovsky, V. E., Sannel, A. B. K., Schuur, E. A. G., and Turetsky, M. R.: Circumpolar distribution and carbon storage of thermokarst landscapes, Nat. Commun., 7, 13043, https://doi.org/10.1038/ncomms13043, 2016.

Patton, A. I., Rathburn, S. L., Capps, D. M., McGrath, D., and Brown, R. A.: Ongoing Landslide Deformation in Thawing Permafrost, Geophys. Res. Lett., 48, https://doi.org/10.1029/2021GL092959, 2021.

Peng, X. and Yang, G.: The hillslope thermokarst invertory for the permafrost region of the Qilian Mountains (2000-2020). National Tibetan Plateau Data Center[data set], https://doi.org/10.11888/Cryos.tpdc.300805, 2023.

Ran, Y., Li, X., Cheng, G., Nan, Z., Che, J., Sheng, Y., Wu, Q., Jin, H., Luo, D., Tang, Z., and Wu, X.: Mapping the permafrost stability on the Tibetan Plateau for 2005–2015, Sci. China Earth Sci., 64, 62–79, https://doi.org/10.1007/s11430-020-9685-3, 2021.

Segal, R. A., Lantz, T. C., and Kokelj, S. V.: Acceleration of thaw slump activity in glaciated landscapes of the Western Canadian Arctic, Environ. Res. Lett., 11, 034025, https://doi.org/10.1088/1748-9326/11/3/034025, 2016.

Sharkhuu, A., Sharkhuu, N., Etzelmüller, B., Heggem, E. S. F., Nelson, F. E., Shiklomanov, N. I., Goulden, C. E., and Brown, J.: Permafrost monitoring in the Hovsgol mountain region, Mongolia, J. Geophys. Res., 112, F02S06, https://doi.org/10.1029/2006JF000543, 2007.

Stephani, E., Darrow, M. M., Kanevskiy, M., Wuttig, F., Daanen, R. P., Schwarber, J. A., Doré, G., Shur, Y., Jorgenson, M. T., Croft, P., and Drage, J. S.: Hillslope erosional features and permafrost dynamics along infrastructure in the Arctic Foothills, Alaska, Permafr. Periglac. Process., 34, 208–228, https://doi.org/10.1002/ppp.2188, 2023.

Stieglitz, M., Déry, S. J., Romanovsky, V. E., and Osterkamp, T. E.: The role of snow cover in the warming of arctic permafrost, Geophys. Res. Lett., 30, https://doi.org/10.1029/2003GL017337, 2003.

Wang, R., Peng, Q., Zhang, W., Zhao, W., Liu, C., and Zhou, L.: Ecohydrological Service Characteristics of Qilian Mountain Ecosystem in the Next 30 Years Based on Scenario Simulation, Sustainability, 14, 1819, https://doi.org/10.3390/su14031819, 2022.

Ward Jones, M. K., Pollard, W. H., and Jones, B. M.: Rapid initialization of retrogressive thaw slumps in the Canadian high Arctic and their response to climate and terrain factors, Environ. Res. Lett., 14, 055006, https://doi.org/10.1088/1748-9326/ab12fd, 2019.

Xia, Z., Huang, L., Fan, C., Jia, S., Lin, Z., Liu, L., Luo, J., Niu, F., and Zhang, T.: Retrogressive thaw slumps along the Qinghai–Tibet Engineering Corridor: a comprehensive inventory and their distribution characteristics, Earth Syst. Sci. Data, 14, 3875–3887, https://doi.org/10.5194/essd-14-3875-2022, 2022.

Xiong, J., Li, Y., Zhong, Y., Lu, H., Lei, J., Xin, W., Wang, L., Hu, X., and Zhang, P.: Latest Pleistocene to Holocene Thrusting Recorded by a Flight of Strath Terraces in the Eastern Qilian Shan, NE Tibetan Plateau, TECTONICS, 36, 2973–2986, https://doi.org/10.1002/2017TC004648, 2017.

Yang, D., Qiu, H., Ye, B., Liu, Y., Zhang, J., and Zhu, Y.: Distribution and Recurrence of Warming-Induced Retrogressive Thaw Slumps on the Central Qinghai-Tibet Plateau, J. Geophys. Res. Earth Surf., 128, e2022JF007047, https://doi.org/10.1029/2022JF007047, 2023.

629   Yin, G., Niu, F., Lin, Z., Luo, J., and Liu, M.: Effects of local factors and climate on
630   permafrost conditions and distribution in Beiluhe basin, Qinghai-Tibet Plateau, China,
631   Sci. Total Environ., 581–582, 472–485,
632   https://doi.org/10.1016/j.scitotenv.2016.12.155, 2017.

633   Yin, G., Luo, J., Niu, F., Lin, Z., and Liu, M.: Machine learning-based thermokarst
634   landslide susceptibility modeling across the permafrost region on the Qinghai-Tibet
635   Plateau, Landslides, 18, 2639–2649, https://doi.org/10.1007/s10346-021-01669-7,
636   2021.

637   YU Hong, J. Z., ZENG Hui: Study on Distribution Characteristics of Landscape
638   Elements along the Terrain Gradient, SCIENTIA GEOGRAPHICA SINICA, 21, 64,
639   https://doi.org/10.13249/j.cnki.sgs.2001.01.64, 2001.

640   Zhang, T.: Influence of the seasonal snow cover on the ground thermal regime: An
641   overview, Rev. Geophys., 43, https://doi.org/10.1029/2004RG000157, 2005.

642